PEPSI's non-detection of escaping hydrogen and metal lines adds to the enigma of WASP-12 b

Anusha Pai Asnodkar [ORCID],[1]★ Ji Wang(王吉) [ORCID],[1] Madelyn Broome [ORCID],[2] Chenliang Huang(黄辰亮) [ORCID],[3] Marshall C. Johnson [ORCID],[1] Ilya Ilyin,[4] Klaus G. Strassmeier[4] and Adam Jensen[5]

[1]*McPherson Laboratory, The Ohio State University, 140 W 18th Avenue, Columbus, OH 43210, USA*
[2]*Department of Astronomy and Astrophysics, University of California Santa Cruz, 1156 High Street, Santa Cruz, CA 95064, USA*
[3]*Shanghai Astronomical Observatory, Chinese Academy of Sciences, Shanghai 200030, People's Republic of China*
[4]*Leibniz-Institute for Astrophysics Potsdam (AIP), An der Sternwarte 16, D-14482 Potsdam, Germany*
[5]*Department of Physics and Astronomy, University of Nebraska at Kearney, 2502 19th Avenue, Kearney, NE 68849, USA*

ABSTRACT

WASP-12 b is an ultra-hot Jupiter of special interest for atmospheric studies since it is on an inspiraling orbit in an extreme environment of intense radiation and circumstellar gas. Previously claimed detections of active mass-loss from this planet are controversial across the literature. To address this controversy, we obtain two new transit observations of WASP-12 b with the optical high-resolution PEPSI spectrograph on the Large Binocular Telescope. Contrary to previous work, we do not observe planetary Hα absorption and rule out the amplitude of previously reported detections. Our non-detection may be limited by the sensitivity of our data or could indicate weaker mass-loss than suggested by previous studies. We conduct injection-recovery experiments to place constraints on the radial extent of WASP-12 b's escaping atmosphere as probed by Balmer lines, but find that our data do not have the sensitivity to probe down to the planet's Roche lobe. Using physically motivated models of atmospheric escape, we explore upper limit constraints on the planet's mass-loss rate and deem the data quality in the wavelength regime of Balmer lines insufficient to determine a physically meaningful constraint. We also conduct a spectral survey of other optical absorbers to trace atmospheric circulation but detect no additional absorption. We conclude that previous claims of Hα absorption from the atmosphere of WASP-12 b should be reevaluated. Given the anticipated line strength of Balmer/optical features, observing the atmosphere of this faint target will require stacking more observations even with the largest telescope facilities available.

Key words: exoplanets – planets and satellites: atmospheres – planets and satellites: gaseous planets – methods: observational – techniques: spectroscopic telescopes.

1 INTRODUCTION

Among the diverse menagerie of exoplanets discovered to date, WASP-12 b (Hebb et al. 2009) is one of the most extreme worlds ($R_p = 1.9 R_{jup}$, $M_p = 1.47 M_{jup}$, $P \approx 1.09$ d, $T_{eq} = 2580$ K; Collins, Kielkopf & Stassun 2017), displaying exotic phenomena unlike anything in our own Solar system. It was the first system to confirm predictions from theory that some close-in giants may have decaying orbits due to tidal interactions with their host stars (Maciejewski et al. 2016; Yee et al. 2020; Turner, Ridden-Harper & Jayawardhana 2021). With an inspiral time-scale of $\leq 2.9 \pm 0.14$ Myr (Efroimsky & Makarov 2022), WASP-12 b is an ideal testbed for probing the tidal quality and, in effect, the interiors of irradiated gas giants (Barker & Ogilvie 2009; Patra et al. 2017; Weinberg et al. 2017; Maciejewski et al. 2018, 2020; Millholland & Laughlin 2018; Bailey & Goodman 2019). Recently, Efroimsky & Makarov (2022) demonstrated that WASP-12 b's orbital decay is consistent with tidal dissipation and

its tidal quality factor is comparable to Jupiter's. Such gravitational influences distort WASP-12 b into a prolate, disrupted planet being devoured by its host star as indicated by the imprint of the planet's geometry on its light curve (Li et al. 2010; Akinsanmi et al. 2024).

Spectroscopic investigation of the WASP-12 system generally corroborates the aforementioned findings. The host star's lack of the line core emission from tracers of chromospheric activity (Mg II h&k and Ca II H&K) that is typical for stars of comparable spectral type (between late-F and early-G) and age (~ 2 Gyr) has been suggested as evidence of additional absorption from a circumstellar torus of material (Haswell et al. 2012; Bonomo et al. 2017; Debrecht et al. 2018; Haswell 2018). This is further supported by WASP-12 b's early ingress near-ultraviolet (near-UV) absorption reported in Fossati et al. (2010), suggesting the disc material is perhaps stripped from the planetary atmosphere, although the possibility of ejected plasma debris from outgassing of a Trojan satellite or exomoon has also been proposed (Haswell et al. 2012; Fossati et al. 2013; Ben-Jaffel & Ballester 2014; Kislyakova et al. 2016; Debrecht et al. 2018). A

★ E-mail: paiasnodkar.1@osu.edu

Table 1. Observing log of WASP-12 b transit observations: columns provide the night number, date of observation, telescope observing mode (default is binocular, but can be monocular in unexpected circumstances), UTC start and end times of observing, number of exposures per night, exposure times in seconds for PEPSI blue and red arms, and average single exposure SNR per pixel for PEPSI blue ($\lambda 4800–5441$) and red arms ($\lambda 6278–7419$).

Night	Date	Observing mode	t_{start} (UTC)	t_{end} (UTC)	N_{obs}	$t_{exp,blue}$ (s)	$t_{exp,red}$ (s)	Airmass	$\overline{SNR}_{blue}$	$\overline{SNR}_{red}$
1	2020-11-22	Binocular	07:12:38.0	13:15:34.6	24	900	900	1.0013–1.451	97.3	135.5
2	2020-12-27	Monocular	04:47:32.2	10:18:53.8	22	900	900	1.0015–1.2761	67.1	94.2

deeper investigation of the planet's atmosphere in the UV during transit provides indirect evidence for the presence of numerous metals (Al II, Fe II, Mg II, Mn I/II, Na I, Sc I, Sn I, V II, and Yb II) in its exosphere, indicative of a hydrodynamic outflow (Fossati et al. 2010; Haswell et al. 2012).

Transmission spectroscopy in the optical at medium resolution ($R\sim15\,000$ with the high-resolution spectrograph (HRS) on the 10-m Hobby–Eberly Telescope, HET) revealed Hα and Na I absorption from the planetary atmosphere, but no Hβ or Ca I (Jensen et al. 2018). Their work remains inconclusive on the radial extent of the $n = 2$ hydrogen population probed by their Hα detection and whether or not the probed atmosphere overfills the planetary Roche lobe, an independent indication of active hydrodynamic escape. More recent work by Czesla et al. (2024) reports no extended atmospheric Hα absorption from transit observations of WASP-12 b with the CARMENES HRS ($R\sim94\,600$) on the 3.5-m telescope at the Calar Alto Observatory. Kreidberg & Oklopčić (2018) report a notable non-detection of helium, another tracer of atmospheric escape, in the planet's exosphere from the metastable triplet feature in the infrared; this non-detection is further supported by Czesla et al. (2024).

In this work, we extend the optical exploration of WASP-12 b's atmosphere to higher resolution ($R\sim130\,000$) and larger telescope aperture (2×8.4 m, with an effective aperture size of 11.8 m) with the PEPSI spectrograph on the Large Binocular Telescope (LBT). Higher resolution can provide clarity on velocity information that is lost at lower resolutions to constrain the dynamics of a planetary outflow as well as circulation in the upper atmosphere. Furthermore, the LBT's larger telescope aperture relative to the HBT and the CARMENES instrument is more sensitive to low signal-to-noise ratio (SNR) planetary signals. We conduct transmission spectroscopy with PEPSI-LBT to follow-up the investigation of Hα in Jensen et al. (2018) as well as other metal species at optical wavelengths. In Section 2, we describe the details of the two transit observations we obtained with PEPSI. In Section 3, we outline our pipeline for reducing the data. In Section 4, we discuss constraints on the hydrogen envelope's radial extent from injection-recovery tests. Similarly, we attempt to place constraints on the planet's mass-loss rate in Section 5. Section 6 describes our search for other optical absorption in WASP-12 b's atmosphere and we discuss our constraints in the context of previous work and other comparable systems. We present our conclusions in Section 7.

2 OBSERVATIONS

We conduct high-resolution transmission spectroscopy of WASP-12 b using the optical Potsdam Echelle Polarimetric and Spectroscopic Instrument (PEPSI; Strassmeier et al. 2015) on the LBT (two 8.4-m mirrors, effective aperture of 11.8 m in binocular mode; Wagner 2008). We use data from cross-dispersers III ($\sim4800–5441$ Å, $R = 130\,000$) and V ($\sim6278–7419$ Å, $R = 130\,000$) for the necessary wavelength coverage to observe Balmer-line features (Hα and Hβ). From the standard PEPSI pipeline (Ilyin 2000; Strassmeier, Ilyin & Steffen 2018), we obtain continuum-normalized, order-stitched 1D

spectra for every exposure, each corrected for solar barycentric motion. These spectra from the pipeline are ready to be directly adopted by the procedure described in Section 3. We analyse two nights of observations in this work; see Table 1 for details about the observations.

Both data sets include observations taken during transit as well as several immediately before and after the transit to establish an out-of-transit baseline. We adopt an exposure time of 900 s for both PEPSI arms. On Night 1, the continuum SNR per exposure ranged between 77 to 113 in the blue arm and 106 to 156 in the red arm. On Night 2, the continuum SNR ranged between 52–77 in the blue arm and 73–107 in the red arm. As indicated in Table 1, Night 2 observations have lower SNR because the LBT was configured in monocular mode for simultaneous observation with the LUCI (Seifert et al. 2003) instrument (these data are not relevant for this work). We converted all observation timings from the provided JD_{UTC} timings into BJD_{TDB} using the Time Utilities[1] online software tool (Eastman 2012) to make them comparable with the ephemeris of the WASP-12 system given in Wong et al. (2022).

3 METHODS

We follow a procedure for transmission spectrum construction similar to that in Pai Asnodkar et al. (2022). To extract transmission spectra of WASP-12 b's atmosphere, we

(i) perform least-squares deconvolution (LSD) to recover stellar radial velocities (RVs),

(ii) perform a Keplerian RV curve fit to recover the orbital properties of the host star,

(iii) shift all observations to the stellar rest frame,

(iv) divide all observations by a combined stellar spectrum constructed from out-of-transit observations,

(v) apply the SYSREM (Tamuz, Mazeh & Zucker 2005) algorithm to remove systematic effects.

We will proceed to describe each of these steps in further detail.

We are interested in the probing the dynamics of the planet's atmosphere. This will require spectroscopically measuring the radial velocity (RV) of the planet's atmospheric absorption signature relative to the orbital motion of the planet. The first step towards achieving this requires shifting to the stellar rest frame to remove the stellar component, which requires knowing the systemic velocity and RV semi-amplitude of the host star. We extract the orbital properties of the host star from the out-of-transit observations taken on both nights of observation using LSD and RV fitting as described in section 3.1 of Pai Asnodkar et al. (2022). First, we generate template spectra of the star in the IDL software SPECTROSCOPY MADE EASY (SME) (Valenti & Piskunov 1996, 2012) at 21 different limb-darkening angles using the VALD3 linelist for a $T_{eff} = 6360$ K star as an input. We integrate across the stellar disc, which we treat as a grid

---

[1] https://astroutils.astronomy.osu.edu/time/utc2bjd.html

of $0.01R_\star \times 0.01R_\star$ cells, and continuum-normalize to construct a stellar template spectrum. We then conduct LSD (Donati et al. 1997; Kochukhov, Makaganiuk & Piskunov 2010) to recover the empirical broadening profiles of the out-of-transit observations of the host star. The broadening kernel includes a Gaussian component from instrumental broadening (Strassmeier et al. 2018) and a rotational broadening component as defined analytically in Gray (2005). We globally fit the empirical profiles with a model that is the convolution of the Gaussian and rotational components. The centroids of the model fit to each empirical profile is the RV of the star at the orbital phase corresponding to the observation. The centroids are determined according to a circular orbital solution:

$$v_\star(t) = K_\star \sin\left(\frac{t - t_0}{p}\right) + v_{\text{sys}}. \tag{1}$$

The free parameters in our model of the line-broadening profiles are the stellar linear limb-darkening coefficient, $v \sin i_\star$, stellar RV semi-amplitude ($K_\star$) and the systemic velocity measured by the PEPSI instrument (v_{sys}). A multiplicative scaling factor and an additive offset are included as nuisance parameters in the fitting. The multiplicative scaling factor rescales the analytical kernel to match the amplitude of the empirical deconvolved line profiles. The additive offset is necessary because the empirical deconvolved line profiles may not have a baseline centred at 0 due to a lack of flux conservation between the template and observed spectra. $K_\star$ and v_{sys} are our parameters of interest for shifting our observations to the stellar rest frame. In our fitting procedure, we restrict the linear limb-darkening coefficient between 0.3867 and 0.4903 according to the range of plausible values given in Claret 2017. Note that linear limb-darkening laws are known to be an oversimplification of stellar intensity profiles. However, this simplified broadening profile is sufficient to determine the centroids of the observed line profiles to constrain $K_\star$ within $\lesssim 0.05 \text{ km s}^{-1}$ uncertainties as described in the proceeding bootstrapping procedure. This uncertainty on $K_\star$, which we use to shift the spectra to the stellar rest frame, is well within the ~ 1–2 km s^{-1} uncertainties on the RV of the planet's atmospheric absorption we expect with PEPSI (Pai Asnodkar et al. 2022).

We apply least-squares fitting to determine the best-fitting parameters. To estimate parameter uncertainties, we bootstrap the residuals of the flat region of the deconvolved kernel, add the samples to the best-fitting model kernel, and refit the line profiles. We obtain a stellar RV semi-amplitude of $K_\star = 0.3288^{+0.0158}_{-0.0392} \text{ km s}^{-1}$ and a systemic velocity of $v_{\text{sys}} = 19.275^{+0.0243}_{-0.0066} \text{ km s}^{-1}$. This is consistent with the $20.62 \pm 1.44 \text{ km s}^{-1}$ reported on the *Gaia* archive (Gaia Collaboration 2021). We caution that our value for $K_\star$ may be skewed since we are limited by the phase coverage of our observations; Collins et al. (2017) report $0.2264 \pm 0.0041 \text{ km s}^{-1}$, which differs from our measurement by 6.3σ. However, this discrepancy in $K_\star$ should not significantly affect the shift to the stellar rest frame over the limited phase coverage of our observations during transit, at least not beyond the measurement uncertainties of the planet's atmospheric dynamics which we can measure within 1–2 km s^{-1} at best as previously mentioned.

Next, we shift all of our spectra for a given night of observation to the stellar rest frame according to our empirically derived orbital parameters of the star. We then take the error-weighted mean of the out-of-transit observations to obtain a combined stellar spectrum. We divide the combined stellar spectrum out of all of our observations to remove the dominant stellar component and reveal the absorption features from the planet's atmosphere in transmission. This operation should yield roughly flat spectra for the out-of-transit observations and potentially spectra with absorption features from the planetary

atmosphere for the in-transit phases. Unlike in Pai Asnodkar et al. (2022), we do not see traces of a Doppler shadow from the Rossiter–McLaughlin effect (McLaughlin 1924; Rossiter 1924) in the resulting transmission spectra since the host star WASP-12 is a slow rotator with $v \sin i_\star = 1.6^{+0.8}_{-0.4} \text{ km s}^{-1}$ (Albrecht et al. 2012). This is consistent with Husnoo et al. (2011); therefore, we do not model the Doppler shadow in subsequent analysis.

In addition to the lack of the Doppler shadow due to slow rotation, another deviation from the data reduction in Pai Asnodkar et al. (2022) is the addition of the SYSREM algorithm to this pipeline. The host star is not a rapid rotator, so we can see deep absorption lines from the stellar photosphere in our observations. Since the scatter in stellar spectral flux across observations is roughly uniform over the wavelengths of observation, the SNR at the core of a stellar absorption feature is significantly lower than in the continuum. As a result, when we divide out the combined stellar spectrum, we obtain noisy residual streaks across observations at the wavelengths corresponding to a stellar absorption line (see Fig. 1). Similar streaks have been observed previously in PEPSI transmission observations of the 55 Cnc system (Keles et al. 2022) and in CARMENES observations of our target system WASP-12 (Czesla et al. 2024).

We attempt to mitigate this undesirable artefact by employing the SYSREM algorithm (Tamuz et al. 2005) to filter out systematics across observations. SYSREM operates like an extension of principle component analysis to iteratively identify linear systematic effects. The performance of the algorithm is determined by two parameters: (1) the number of systematics being identified and (2) the number of chi-squared minimization iterations for each systematic. As shown by the vertical streaks in Fig. 1, this procedure is insufficient to completely remove the artefact. However, it is more effective at removing systematics across cross-correlated data (see Section 6.1). Furthermore, the streak is relatively stationary in velocity space around 0 km s^{-1} (since the observations have been shifted to the stellar rest frame and, in general, the star should be close to stationary in the context of the velocities spanned in Fig. 1) while the planet's absorption signature should range roughly between –60 and 60 km s^{-1} over the course of its transit across the stellar disc (assuming no additional RV shifts from atmospheric dynamics). Thus, we expect these two signatures to be distinct in velocity space and we should still be able to see traces of the planet's atmospheric absorption if any such features are sufficiently high signal. For example, fig. 3 of Mounzer et al. (2022) shows an example of excess sodium absorption from KELT-11 b's atmosphere during transit in spite of an obstructive stellar line core artefact.

SYSREM also minimizes telluric contamination because the spectra are shifted by at most $\sim 0.42 \text{ km s}^{-1}$ relative to each other to convert from Earth's rest frame into WASP-12's stellar-frame, so telluric absorption is relatively stationary across observations. Furthermore, tellurics are more prevalent in the PEPSI red arm observations, which we only use to search for Hα absorption, a feature in a wavelength window relatively free of strong tellurics (Smette et al. 2015). We only use blue arm observations (in which tellurics are negligible) for the cross-correlation analysis in Section 6.1. Thus, tellurics are not a significant concern in this work.

4 CONSTRAINING THE RADIAL EXTENT OF WASP-12 B'S HYDROGEN ENVELOPE

4.1 Balmer-line absorption

Since ultra-hot Jupiter (UHJs) like WASP-12 b experience stellar irradiation that is strong enough to thermally dissociate molecular
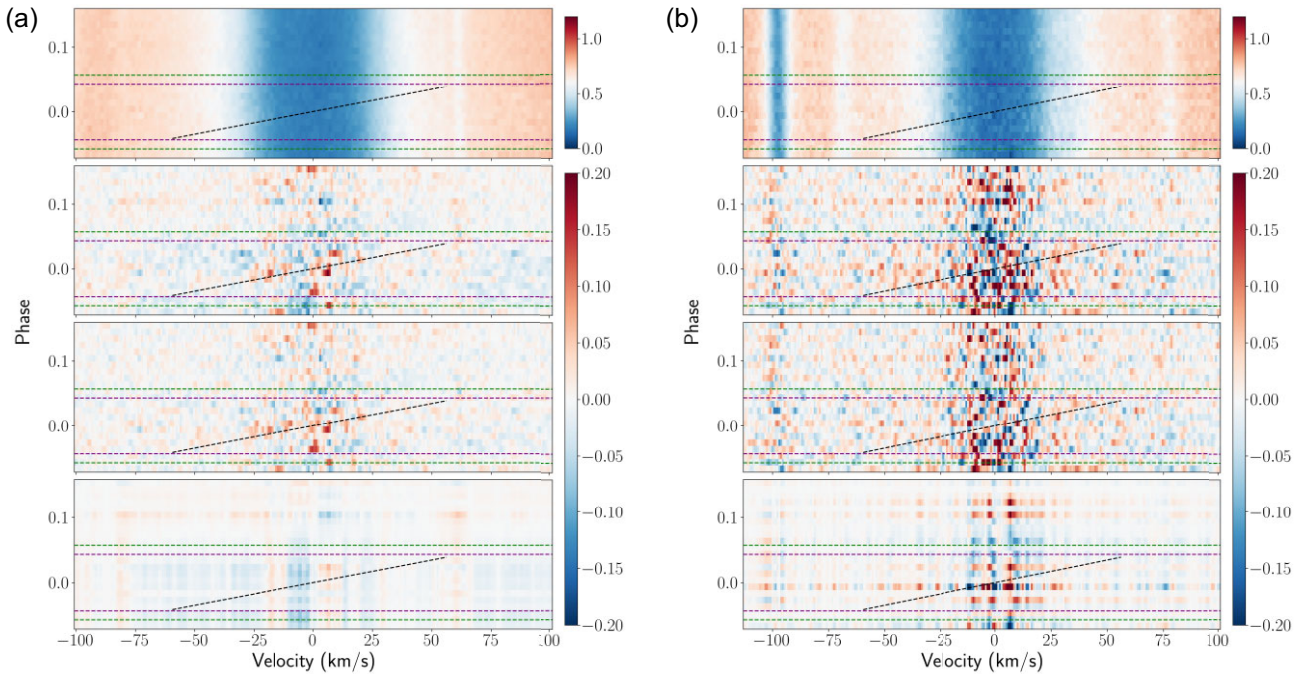
Figure 1. Panel (a): non-detection of planetary atmospheric absorption around Hα line (6562.83 Å) in Night 1 data. The top panel are the order-stitched, continuum-normalized stellar spectra from the PEPSI pipeline where the colour bar represents flux after continuum normalization. The second panel are the spectra with the stellar component removed, i.e. the out-of-transit combined stellar spectrum has been divided out and the result is subtracted by 1 such that the baseline flux of the star fluctuates around zero; red (values greater than zero) indicates excess emission while blue (values less than zero) indicates excess absorption. The third panel shows the spectra from the second panel after applying SYSREM (2 systematics, 100 iterations per systematic). The fourth and bottom panel displays the difference between the second and third panels. In all panels, the green horizontal dashed lines indicate the phases of first and fourth contact of transit while the purple horizontal dashed lines indicate the phases of second and third contact. The black-dashed line maps out the planet's expected orbital RV over the course of its transit based on the system parameters provided in Collins et al. (2017). The assignment of orbital phases to each observation is dependent on our adopted mid-transit timing from Wong et al. (2022), which has an uncertainty of 6.22 s. If the mid-transit time were off by 1σ, it would shift the track horizontally by $\sim$0.1 km s^{-1}. Panel (b): same as (a), but around Hβ line (4861.34 Å).

hydrogen, neutral hydrogen is expected to be a dominant species in their upper atmospheres. Hydrogen Balmer lines in planetary atmospheres can probe neutral hydrogen at high altitudes and the escape regime (Jensen et al. 2018; Yan & Henning 2018; Casasayas-Barris et al. 2019; Cauley et al. 2019; Cabot et al. 2020a; Yan et al. 2021). In our wavelength regime with PEPSI cross-dispersers III and V, we can observe the Hα (6562.83 Å) and Hβ (4861.34 Å) features (Wiese & Fuhr 2009). Just by eye, we do not observe any excess absorption attributable to planetary absorption around either of these wavelengths (see e.g. Fig. 1); likewise, we do not observe planetary Balmer-line absorption in publicly available archival HARPS-North transit data sets (2017 December 23 and 2018 November 14).[2] We attempt a quantitative recovery of Balmer-line signals in transmission using Bayesian parameter estimation and a model of the planet's atmospheric absorption that is described further in Section 4.2, but still recover no signal. This is consistent with the absence of atmospheric Hα absorption from CARMENES data reported in Czesla et al. (2024), but in tension with the strong detection in Jensen et al. (2018). See Section 4.2 for a quantitative framework for placing upper limit constraints on the radial extent of WASP-12 b's hydrogen envelope.

We note that Kreidberg & Oklopčić (2018) and Czesla et al. (2024) report non-detections of helium, another commonly adopted tracer of atmospheric escape. It has been noted that the metastable helium

triplet can be insufficiently populated for atmospheres receiving low extreme-UV and X-ray irradiation from their host stars (Sánchez-López et al. 2022a). However, this is unlikely to be applicable to WASP-12 b considering the helium triplet has been observed in HD 209 458 b (Alonso-Floriano et al. 2019), which orbits a G0 star of a similar spectral type as WASP-12 b's host. On the other hand, the UV flux of the host star WASP-12 may be anomalous for its spectral type as indicated by its lack of emission in the line cores of the Mg II h&k stellar activity tracers (Fossati, Haswell & Froning 2011), although this has also been speculatively attributed to absorption from a circumstellar disc of escaping gas from the planet or potential Trojan satellites. The metastable state of helium can also be depopulated in the most extreme UHJ atmospheres (like WASP-12 b) exposed to high near-UV flux (Oklopčić 2019).

4.2 Injection-recovery analysis of Balmer lines

Although we do not observe any excess Balmer absorption from the planetary atmosphere during transit, we place upper limit constraints on the radial extent of WASP-12 b's hydrogen envelope based on the noise properties (scatter of the transmission spectra with the stellar component divided out) of our data sets. The aim of this is to determine if the planet's atmosphere is confined within its Roche lobe (Eggleton 1983) and is thus unlikely to be in the regime of strong hydrodynamic escape. We conduct an injection-recovery analysis, modelling planetary absorption observed with transmission spectroscopy as a Gaussian feature broadened by instrumental effects.
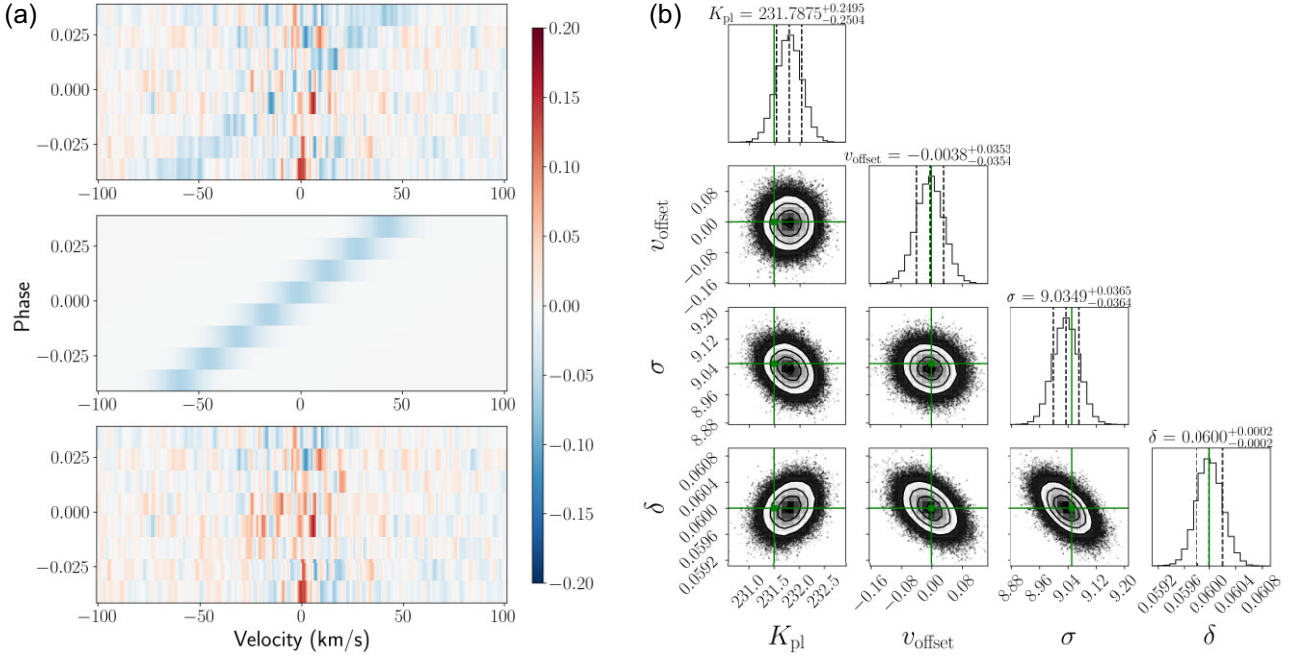
[2] http://archives.ia2.inaf.it/tng/

Figure 2. Panel (a): injection (top panel), recovery (model fit in middle panel), and residuals (difference map between injected data and model fit, bottom panel) of a planetary Hα signal comparable to the detection in Jensen et al. (2018). Note that this plot is showing a simulated Hα feature incorporating the noise of our spectroscopic observations and does not depict a true, measured absorption feature in our PEPSI data. As in Fig. 1, red indicates excess emission and blue indicates excess absorption. Panel (b): corner plot of parameter posterior distributions from MCMC sampling. The green lines identify the true injected parameters and fall within the 1σ regime of the sampled distributions, indicating that the injected signal is successfully recovered. The injected signal is retrieved with an SNR of 5σ.

Note that the true line profile from a hydrodynamic outflow will not be a pure Gaussian due to a combination of thermal, rotational, instrumental, and outflow expansion velocity broadening effects. However, we do not expect the precise line shape of the model to significantly affect our injection-recovery analysis given the data quality.

We first generate Gaussian signals to represent the planet's Balmer-line absorption. Adopting the system parameters from Collins et al. (2017), the translation from atmospheric radial extent R_{ext} to the depth of the Gaussian absorption feature δ is

$$\delta = \frac{R_{\text{ext}}^2 - R_{\text{p}}^2}{R_{\star}^2}. \tag{2}$$

The widths of the Gaussian signals we inject are motivated by limits taken from observations and models of other UHJs. Across the literature, the observed full width at half-maximum (FWHM) of Balmer absorption from an UHJ ranges from ~ 20 to $50\,\text{km}\,\text{s}^{-1}$ (Casasayas-Barris et al. 2019; Wyttenbach et al. 2020; Borsa et al. 2021; Zhang et al. 2022). We take $20\,\text{km}\,\text{s}^{-1}$ as the lower limit and adopt $60\,\text{km}\,\text{s}^{-1}$ as the upper limit on the FWHM of the signals we inject according to a multispecies hydrodynamic model of a WASP-121 b (Huang et al. 2023), a planet with properties very similar to WASP-12 b. The Gaussian signal is convolved in a flux-conserving manner (constant equivalent width) with an instrumental broadening kernel. PEPSI's instrumental broadening is captured by a Gaussian kernel with an FWHM in velocity units of $\frac{c}{R}$, where c is the speed of light and R is the spectral resolution of the data ($R = 130\,000$). The resulting signal is subtracted from 1 (continuum) and injected (multiplied) into our normalized observations as an Hα or Hβ absorption feature, where the centre of the signal is offset from the central wavelength according to the radial orbital motion of the

planet; this offset calculation is analogous to equation (1), except the planet's projected orbital velocity (K_{pl}) is used in place of $K_{\star}$ and the planet's net RV offset in the stellar rest frame (set to 0 km s^{-1}) is used instead of v_{sys}. In doing so, the noise properties of the observations are incorporated in the simulated data. We assume the planet's orbital motion is circular with projected orbital velocity $K_{\text{pl}} = \frac{2\pi a_{\text{pl}}}{P} = 231.7\,\text{km}\,\text{s}^{-1}$ based on orbital parameters from Wong et al. (2022) and that there are no additional velocity offsets from atmospheric dynamics.

To find the upper limit constraint on the planet's radial extent, we use the root-finding routine (SCIPY.OPTIMIZE.ROOT) to minimize R_{ext} until the SNR of the injected feature in the simulated data is at least 3. To calculate SNR, we first stack all in-transit simulated observations in the planet's rest frame. We define SNR of the resulting stacked absorption feature as follows:

$$\text{SNR} = \frac{A}{\text{RMS} \times \text{FWHM}}. \tag{3}$$

In equation (3), the signal A is the planetary absorption signal in the simulated data subtracted from the continuum and integrated over the velocity range that spans the FWHM of the signal. The denominator captures the noise, in which RMS is the root mean square (RMS) error of the residuals within the FWHM of the signal, i.e.

$$RMS = \sqrt{\frac{\sum_{i=1}^{N}(\text{data}_i - \text{model}_i)^2}{N}} \tag{4}$$

for N data points across the FWHM of the absorption line in all in-transit observations. To make the noise an area comparable to the integral, we use for estimating the signal in equation (3), we scale the RMS by FWHM, which is the FWHM of the absorption line.
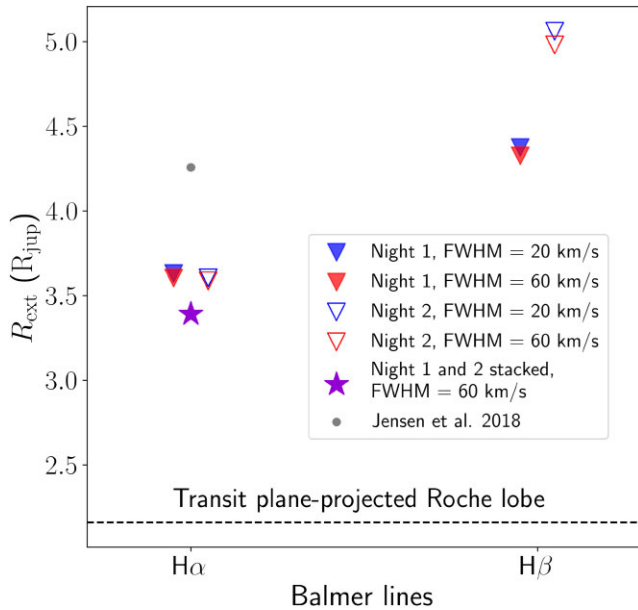
Figure 3. Upper limits (3σ) on WASP-12 b's hydrogen envelope compared to (1) the planet's Roche lobe projected on to the transit plane as perceived with transmission spectroscopy and (2) Hα radial extent reported in Jensen et al. (2018).

To ensure the injected 3σ signals can be retrieved amidst the observational noise, we perform model fitting with MCMC sampling using EMCEE (Foreman-Mackey et al. 2013); see Fig. 2. The model that we fit to the simulated data is the same model used to generate the injected signal. We adopt a Bayesian framework for sampling the parameter space with MCMC applying linearly uniform priors and marginalize over model parameters, i.e. K_{pl} (planet RV semi-amplitude), v_{offset} (net RV offset of signal relative to the stellar rest frame), σ (Gaussian width), and δ (absorption depth) as shown in Fig. 2 as an example. The ability to recover the injected model parameters is limited by the noise quality of the data. We use $-\frac{\chi^2}{2}$ as the log-likelihood of a given model and scale the priors by the number of elements in the observed flux map before summing the log-prior and log-likelihood to obtain the log-posterior probability. We run the EMCEE sampler with 10 walkers until the following convergence criteria are met (1) the estimated autocorrelation time is 1 per cent of the chain length and (2) the estimated autocorrelation time has changed by less than 1 per cent, checking every 100 steps. We consider a signal successfully recovered if the posterior distributions of all parameters appear sufficiently Gaussian or converged.

Fig. 3 provides a summary of our upper limits on WASP-12 b's hydrogen envelope as probed by Hα and Hβ for both nights of observation.

4.3 Upper limits on WASP-12 b's excited-state hydrogen radial extent are above the planet's Roche lobe

We define the lowest value of R_{ext} that yields a 3σ signal as our empirical upper limit constraint on the radial extent of WASP-12 b's hydrogen envelope (see Fig. 3). The disparity in the upper limit constraints on radial extent between different absorption features and data sets arises from the empirical noise corresponding to the wavelength regime of that feature for that night of observation. It is worth noting that the noise in the red arm observations near the wavelength regime of Hα is very similar for both nights of

observation, while the blue arm observations near Hβ have larger scatter (by a factor of $\sim$1.5) in Night 2 observations than Night 1; this is why both nights yield similar upper limits on radial extent probed by Hα, but a smaller radial extent from Hβ with Night 1 data than Night 2. Since the blue arm is generally noisier than the red arm, we get tighter constraints from the Hα upper limits than Hβ.

From Fig. 3, it is evident that for individual nights of observation, we are unable to constrain the radius of the planet's neutral hydrogen envelope down to its Roche lobe given our data quality. In this situation, the planet may have a hydrodynamically escaping atmosphere that extends beyond the Roche lobe but below our sensitivity, or it may have a weakly escaping atmosphere confined within the Roche lobe. As indicated by the purple star in Fig. 3, even when we stack both nights, we find that at best the FWHM = 60 km s^{-1} scenario is observable in Hα with $\geq 3\sigma$ confidence if $R_{ext} \geq 3.39 R_{jup}$, which is well above WASP-12 b's transit plane-projected Roche lobe of $2.16 R_{jup}$.

The true conditions (temperature and hydrogen number density) in WASP-12 b's upper atmosphere remain elusive due to the absence of an observable absorption signature, so we are unable to conclusively make a statement about the status of WASP-12 b's atmospheric escape from our upper limit constraints on its Balmer-line photosphere. In Section 5, we investigate the possibility that WASP-12 b's mass-loss may be much weaker than expected based on other UHJs.

4.4 Tension with Jensen et al. (2018)

We inject an Hα signal of a similar strength as the detection in Jensen et al. (2018) measured with the HRS (Tull 1998) on the HET (Ramsey et al. 1998; Hill et al. 2021), in our Night 1 observations; see Fig. 2. We set the absorption depth to 0.06 based on fig. 9 of Jensen et al. (2018). We choose a Gaussian standard deviation corresponding to the planet's rotational velocity (assuming the planet is tidally synchronous with the star) at R_{pl} (9.05 km s^{-1}). This is narrower than any width we consider in our injection-recovery analysis in Section 4.3 and amounts to a width of $\sim$0.2 Å; the equivalent width of the signal we inject is –29.8 mÅ, which is less than half the equivalent width of WASP-12 b's Hα signature of –64.9 mÅ reported in Jensen et al. (2018). Note that a real signal would appear narrower and deeper in PEPSI data than the HRS data from Jensen et al. (2018) because PEPSI ($R\sim$ 130 000) is higher resolution than HRS ($R\sim$ 15 000); however, instrumental broadening preserves total flux, so the equivalent width of both signals should be the same. Since our injected signal's equivalent width is less than that of the Hα feature presented in Jensen et al. (2018), it should be more challenging to recover. Nevertheless, we are able to retrieve this signal with an SNR of 5σ. Therefore, we have the data quality to detect an Hα absorption feature with the same properties as the strong signal detected in Jensen et al. (2018), so our incongruent lack of such a detection challenges the collective understanding of the WASP-12 system across the literature.

To explore this discrepancy with Jensen et al. (2018) in further detail, we run their Hα observations from HRS through our data analysis pipeline. Our extraction of the transmission spectrum can be seen in Fig. 4. Since these data are not uniformly sampled in phase, we present the spectra in order of increasing phase from bottom to top. The horizontal green-dashed lines indicate first and fourth contact; thus observations between these lines were taken during transit. We correct for the 18.75 km s^{-1} systemic RV adopted in Jensen et al. (2018) according to Gaia Collaboration (2016). These data present a potentially transit-correlated absorption signal as indicated by the
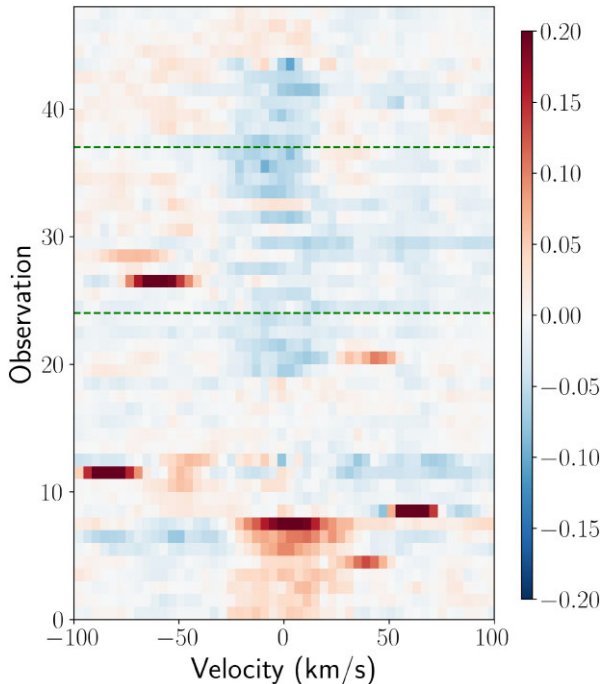
We note that this code is intended for modelling metastable He absorption (Oklopčić & Hirata 2018) and does not include a routine for estimating Balmer series population levels. For this reason, we primarily use P-WINDS to estimate the outflow structure (velocities and individual species number densities as a function of radius) for a given mass-loss rate. For this step, we: (1) use the planetary parameters from Collins et al. (2017), (2) assume a hydrogen number fraction of 0.9, (3) assume solar abundances of carbon and oxygen (the two metal species included this model), and (4) scale the solar high-energy spectrum[3] for WASP-12 b's orbital configuration to estimate the wavelength-dependent photoionizing instellation upon the planet. We also enable P-WINDS's functionality to include tidal effects since WASP-12 b's mass-loss is expected to be dominated by Roche lobe overflow (Koskinen et al. 2022). Then we adopt the Monte Carlo-based framework in Huang et al. (2017) to estimate the $n = 2$ state number densities from equation (14) of Huang et al. (2017). We provide the Balmer series number density structure as an input to the P-WINDS radiative transfer routine, along with the microphysical parameters (central wavelength, oscillator strength, and Einstein coefficient from Wiese & Fuhr 2009) of Hα and Hβ instead of the metastable helium triplet as originally intended. We generate models for two different mass-loss cases, $\dot{M}_{pl} = 10^{10}$ g s^{-1} (weak) and $\dot{M}_{pl} = 10^{12}$ g s^{-1} (moderate). The moderate mass-loss case is defined based on observed mass-loss rates of other UHJs, like KELT-9 b and KELT-20 b, which range between 10^{12} and 10^{13} g s^{-1} (Yan & Henning 2018; Wyttenbach et al. 2020; Huang et al. 2023). Furthermore, a hydrodynamic escape code we adopt (see Section 5.3) predicts a mass-loss rate of $\sim 4 \times 10^{12}$ g s^{-1} for this system.

After generating Balmer absorption signals with P-WINDS, we inject them in our observations to place upper limits on WASP-12 b's mass-loss rate. As in Section 4.2, we apply instrumental broadening to the signal before injection. We also perform rotational broadening since the 1D escape code does not incorporate the line-of-sight effects from planetary rotation. We follow section 4.3 of Huang et al. (2023) and build a rotational broadening kernel corresponding to the planetary rotational velocity at R_{ext} assuming WASP-12 b is tidally locked with its host star and obeys rigid body rotation. Since transmission spectroscopy only probes the transparent terminator region of the planet's atmosphere, we define the rotational broadening kernel $L_{rot}(v)$ such that the value at a given line-of-sight projected rotational velocity of the planet v is weighted by the cross-sectional length of the atmosphere illuminated at that velocity, i.e.

$$L_{rot}(v) = \begin{cases} \sqrt{R_{ext}^2 \left(1 - \frac{v^2}{v_{rot}^2}\right)} - \sqrt{R_{core}^2 - \frac{R_{ext}^2 v^2}{v_{rot}^2}} & \text{if } \frac{R_{ext}v}{v_{rot}} < R_{core} \\ \sqrt{R_{ext}^2 \left(1 - \frac{v^2}{v_{rot}^2}\right)} & \text{if } \frac{R_{ext}v}{v_{rot}} \geq R_{core}. \end{cases}$$
(5)

Here, v_{rot} is the line-of-sight projected rotational velocity of the planet (we assume it is tidally locked) at R_{ext}. We adopt the approximation $R_{core} \approx R_{pl}$ because R_{core} is the radius at which the planet is opaque to all wavelengths. For R_{ext}, we fit the absorption feature that comes out of P-WINDS (before applying velocity broadening from the outflow's expansion) with a Gaussian model to estimate δ and inverting equation (2) to solve for R_{ext}, then apply equation (5). We convolve the expansion velocity-broadened signal from P-WINDS with the rotational broadening kernel and instrumental kernel in a flux-conserving manner (constant equivalent width) for completeness, although we find neither of these broadening effects significantly

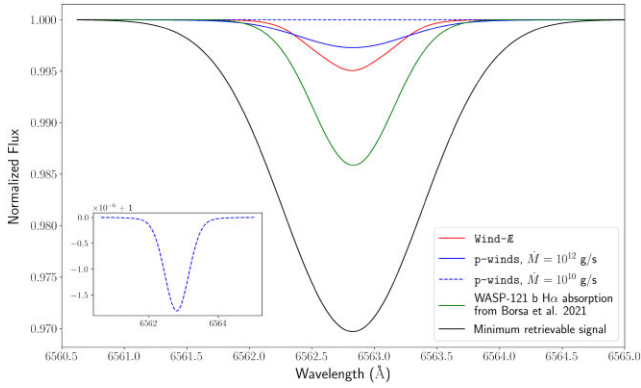[3]https://raw.githubusercontent.com/ladsantos/p-winds/main/data/solar_spectrum_scaled_lambda.dat

Figure 4. Transmission spectra using the HET data sets from Jensen et al. (2018), extracted by our pipeline. As in Fig. 1, red indicates excess emission and blue indicates excess absorption. Horizontal green-dashed lines correspond to first and fourth contact.

blue streak. However, this signal is stationary in RV, whereas a signal from a close-orbit planet like WASP-12 b should span a range of RVs between ~ -60 and 60 km s^{-1} over the course of its transit due to the planet's orbital motion. Furthermore, the absorption depth is a factor of $\sim$4 to 12 times deeper than we expect from atmospheric escape models and what is observed from similar systems (see Section 5). While it may have planetary origins that can be explained by exotic physical mechanisms, we believe this signature is the residual from the removal of the noisy stellar line core, much like the artefact we see in our PEPSI transmission spectra for this system. This is not addressed in Jensen et al. (2018). Thus while these data do appear to present potentially astrophysical signals, we believe the planetary origin of this signal remains to be determined and presents a challenge to theoretical models of atmospheric escape.

5 UPPER LIMIT CONSTRAINT ON HYDROGEN MASS-LOSS RATE

5.1 Model injection-recovery with P-WINDS

The primary quantity of interest in studies of atmospheric escape is the mass-loss rate of the planetary atmosphere ($\dot{M}_{pl}$), which can shape the evolution of a planet over the course of its lifetime if sufficiently high. Constraining this mass-loss rate requires a physically motivated model of the outflow structure and a radiative transfer scheme for estimating transmission spectroscopy signals. We adopt the open-source code P-WINDS (Dos Santos et al. 2022) for this purpose. This code assumes the outflow can be approximated by an isothermal, purely H–He Parker wind and solves for steady-state ionization balance. It also includes a module for ray-tracing and radiative transfer to calculate the in-transit spectrum.

Figure 5. Hα absorption feature calculated by P-WINDS for the weak (10^{10} g s^{-1}, dashed blue, see the inset) and moderate (10^{12} g s^{-1}, solid blue) mass-loss rates as well as WIND-Æ (red) compared to the minimum retrievable signal (black, arbitrary width) from the Night 1 data set. We also include the best-fitting model of WASP-121 b's empirical Hα absorption (green) from Borsa et al. (2021) for comparison with observations of a similar system.

Table 2. SNRs from atmospheric escape model injection-recovery tests.

Injected Hα model	SNR
P-WINDS, $\dot{M} = 10^{12}$ g s^{-1}	0.369
WIND-Æ	0.676
WASP-121 b empirical Hα absorption from Borsa et al. (2021)	1.434

impact the depth or shape of the signal. Then we inject the signal into our observations assuming it is shifted in velocity by the projected orbital motion of the planet exclusively. The injected data are fit with the model used in Section 4. The signal is considered observable if it is recovered with SNR > 3.

5.2 Upper limits on WASP-12 b's mass-loss rate from P-WINDS are inconclusive

From our injection-recovery analysis, we find that, under the assumptions of the P-WINDS model, we are unable to recover a Hα signal for either mass-loss case; we adopt the same SNR metric as in Section 4.2. Fig. 5 shows the Hα absorption feature (the stronger of the two Balmer features we model) calculated by P-WINDS for the two mass-loss cases according to the procedure described in Section 5.1. The absorption signature for either mass-loss case is weaker than the minimum amplitude signal with a comparable width (for this we adopt the signal corresponding to the purple star in Fig. 3) that is retrievable at the 3σ level given our data quality. As expected, we find that the modelled Hβ feature is weaker than the Hα feature and thus would make a detection of Hβ more challenging than a detection of Hα. The Hβ/Hα line depth ratio is 0.153 for the $\dot{M} = 10^{12}$ g s^{-1} model and 0.138 for the $\dot{M} = 10^{10}$ g s^{-1} model. Consequently, neither of the mass-loss cases is observable in either Hα or Hβ. This is also highlighted in Table 2, which reports an SNR of 0.369 for the moderate mass-loss P-WINDS model.

Given the lack of observability of Balmer features inferred from this injection-recovery analysis, we cannot use our P-WINDS models to place a meaningful constraint on WASP-12 b's mass-loss rate. We do not attempt to increase the mass-loss rate further to find a 3σ upper limit on our constraint because WASP-12 b's mass-loss rate is expected to be around $\dot{M}_{pl} = 10^{11.4}$ g s^{-1} in an energy-limited

framework (Ehrenreich & Désert 2011). Ehrenreich & Désert (2011) estimate mass-loss rates of the known transiting planets at the time of publication (including WASP-12 b) to be between 10^6 and 10^{13} g s^{-1}, so we do not find it meaningful to attempt to constrain a higher mass-loss rate than what we consider as an upper limit.

Additionally, the models presented thus far have many limitations as a consequence of certain simplifications:

(i) By employing P-WINDS, we assume the outflow can be represented as a 1D, isothermal Parker wind. In reality, the outflow is 3D and likely has a spatially varying temperature gradient that can span thousands of Kelvin over the transit volume that we probe.

(ii) The P-WINDS code does not account for molecular hydrogen, although this may not be a severe drawback since the extreme temperatures in the escape regime suggest any molecular hydrogen should be largely thermally dissociated.

(iii) We approximate the high energy installation upon the planet using the solar spectrum ($T_{eff} = 5777 \pm 10$ K, Smalley 2005), which has a notably lower effective temperature than WASP-12 ($T_{eff} = 6360^{+130}_{-140}$ K, Collins et al. (2017)).

(iv) While they make up a very small fraction of the atmospheric composition, metals do play a critical role in cooling and regulating the temperature structure of the outflow. The only metals accounted for in the P-WINDS model are carbon and oxygen. Furthermore, we assume solar abundances of carbon and oxygen.

(v) One major criticism of our models is that they require extreme temperatures to support physically plausible mass-loss rates (our weak and moderate cases). For example, the lowest isothermal temperature profile at which P-WINDS converges to a solution for the moderate mass-loss case is at a temperature of 13 000 K; for the weak mass-loss case, it is closer to 11 000 K. These temperatures are unexpectedly high by a factor of ∼2 compared to expectations from hydrodynamic escape codes (see the solid orange curve in Fig. 6b). Ionization at such implausibly high temperatures is dominated by thermal (collisional) ionization, which is not included in P-WINDS, rather than photoionization. Furthermore, a higher temperature increases the Lyman-α emissivity in the atmosphere and may artificially inflate the model atmosphere, both of which can result in a larger Hα transit depth. In reality, the absorption signals may be even weaker in amplitude if the physical conditions permit a lower temperature.

5.3 Model injection-recovery with an upcoming multispecies relaxation code (WIND-Æ) provide a tentative upper limit

We adopt another code under development to model WASP-12 b's atmospheric escape with a more realistic (e.g. non-isothermal, multispecies, multifrequency) and flexible (e.g. tunable system parameters, fast) treatment of the outflow structure. WIND-Æ (Broome et al., submitted) is a fast 1D photoionization atmospheric escape code adapted from Murray-Clay, Chiang & Murray (2009). It is a relaxation code with new multispecies and multifrequency capabilities that models atmospheric escape as a transonic Parker wind. We expect WIND-Æ to yield more realistic outflow models than P-WINDS because it does not assume an isothermal atmosphere and can incorporate more metal species which significantly shape the thermal profile.

Boundary conditions for WASP-12 b include $T(R_{min}) = 1000$ K, $\rho(R_{min}) = 5.67 \times 10^{-10}$ g cm^{-3}, where T is temperature and ρ is mass density at the user-defined minimum radius $R_{min} = 1.02 R_{pl}$. We use the following planetary parameters: $M_{pl} = 1.47 M_{jup}$, $R_p = 1.94 R_{jup}$, $M_* = 1.43$ M$_\odot$, and $a = 0.02$ au, which are the planet mass, planet radius in the UV, stellar mass, and semimajor axis
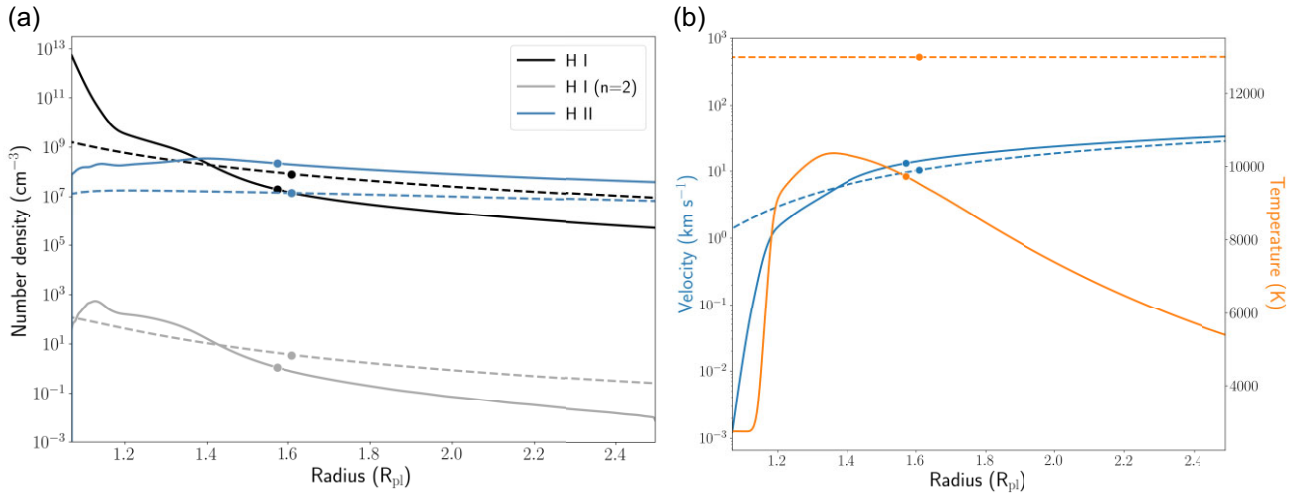
Figure 6. Radial profiles of Panel (a) hydrogen species number density and Panel (b) outflow velocity and temperature for the WIND-Æ model in the solid curves and the $\dot{M} = 10^{12}\,\text{g}\,\text{s}^{-1}$ P-WINDS model in the dashed curves. The circular points mark the sonic point for the respective model of the curve they lie upon.

respectively (Chakrabarty & Sengupta 2019). We adopt an XUV range (10–2000 eV) flux of $F_H = 6.063 \times 10^4\,\text{erg}\,\text{cm}^{-2}\,\text{s}^{-1}$ for scaling the solar spectrum (Chamberlin et al. 2020) to approximate the high energy spectrum of WASP-12. Note that some of these parameters, for example, planetary radius, differ slightly from other parameters used in the P-WINDS model, for which we exclusively use the planet parameters derived in Collins et al. (2017) (listed in Table 3). However, these differences are not significant enough to drastically change the resulting outflow models.

We assume solar metallicity (Lodders, Palme & Gail 2009) and adopt the following species for the composition of the atmosphere: H, He, C, N, O, Ne, Mg, Si, and Ca. We first generate fully self-consistent models out to $\sim 2.5 R_p$, the Coriolis turning radius of the planet; beyond this point, the assumption of spherical symmetry is no longer valid because the outflow no longer travels perpendicular to the planet's surface, but rather is turned by the Coriolis force into a tail. The planetary outflow is also subject to additional physics that we do not model at larger radii, such as charge exchange with the stellar wind which will dominate the energy and ionization of the planetary wind (P-WINDS also do not incorporate these effects). With these caveats in mind, we attempt to integrate the WIND-Æ model profile out to $20 R_p$ to match the radial range of the previous P-WINDS models. To facilitate the integration, it was necessary to artificially inflate the sonic point column density boundary condition by a factor of 2, corresponding to a difference in the resulting model mass-loss rate of 6.4 per cent and near-negligible structural differences in the wind profile compared to the fully self-consistent number density model extending out to $2.5 R_p$. Upon conducting radiative transfer to model the Balmer lines, the discrepancy between the self-consistent $2.5 R_p$ model and the more unphysical $20 R_p$ model was negligible relative to observational uncertainties, so for the purposes of our investigation, we adopt the fully self-consistent $2.5 R_p$ model.

With WIND-Æ, the modelled planetary outflow has a mass-loss rate of $\dot{M} = 3.953 \times 10^{12}\,\text{g}\,\text{s}^{-1}$ with the sonic point at $1.554 R_p$. In contrast to the P-WINDS models, the $H\beta/H\alpha$ line depth ratio from WIND-Æ is 0.267. A comparison of the hydrogen number density, wind velocity, and temperature profiles of WASP-12 b's outflow as modelled by WIND-Æ (solid curves) and P-WINDS (dashed curves) is provided in Fig. 6. Notably, WIND-Æ can incorporate more metal species and a more realistic, radially varying temperature profile,

lending more credibility to the model. In spite of these differences, it is interesting to note that the sonic point and velocity profiles at larger radii are not significantly discrepant between WIND-Æ ($R_s = 1.571 R_{pl}$) and P-WINDS ($R_s = 1.609 R_{pl}$ for $\dot{M} = 10^{12}\,\text{g}\,\text{s}^{-1}$; $R_s = 1.587 R_{pl}$ for $\dot{M} = 10^{10}\,\text{g}\,\text{s}^{-1}$). Since these models incorporate tidal effects, the sonic point should be close to the L1 point, which is at $1.69 R_{pl}$ for WASP-12 b.

The $H\alpha$ feature resulting from the WIND-Æ model, given by the red curve in Fig. 5, is deeper than both the P-WINDS models, but does not fall below the minimum retrievable signal in black. When injected in our data from both nights, it corresponds to an SNR of 0.676 and is thus is not observable with our data quality. Notably Czesla et al. (2024) place an upper limit on WASP-12 b's mass-loss rate of $\lesssim 4 \times 10^{12}\,\text{g}\,\text{s}^{-1}$, similar to the mass-loss rated derived by WIND-Æ, from their non-detection of helium. However, we have shown that we do not have the data quality to validate this upper limit due to substantial photon noise in the optical with PEPSI/LBT. This may suggest that Balmer lines do not produce planetary spectral absorption signatures that are strong enough to be observed with current telescope facilities for a target as faint as the WASP-12 system ($V = 11.569$).

We also compare with the observed $H\alpha$ absorption signal of WASP-121 b from Borsa et al. (2021). To first order, the WASP-121 system is very similar to WASP-12 in terms of the spectral type and age (although poorly constrained, but very likely on the main sequence) of the host star as well as the equilibrium temperature and surface gravity of the planet. Consequently, we expect similar planetary outflow dynamics for the two systems. As indicated by the green curve in Fig. 5 and the SNR of 1.434 reported in Table 2, if WASP-12 b possessed an $H\alpha$ signature comparable to that of WASP-121 b, the absorption feature would be insufficient to detect with both nights of our PEPSI observations stacked. Additionally, both the P-WINDS and WIND-Æ models fall short of the observed $H\alpha$ transit depth of WASP-121 b as seen in Fig. 5. This motivates further validation of both codes, since WASP-121 b's absorption features (including $H\alpha$) were successfully modelled with a robust, multispecies framework in Huang et al. (2023). When compared to our WIND-Æ models of WASP-12 b, the models of WASP 121 b in Huang et al. (2023) display a shallower decrease in pressure below the temperature peak, resulting in a more inflated $H\alpha$ transit depth. Determining the root cause of this difference is beyond this

scope of this observational work, and we recommend a future code comparison paper of atmospheric escape models commonly used in the field.

6 SPECTRAL SURVEY OF ATOMIC AND MOLECULAR FEATURES

6.1 Spectral survey of other atomic and molecular features via cross-correlation

We also search for other optical absorbers commonly observed in UHJ atmospheres, namely metal species such as Fe I/II, Ti I/II, Cr I/II, and potential agents of thermal inversions such as TiO and VO. We scour the wavelength range between 4900 and 5400 Å to avoid broad Hβ absorption at lower wavelengths and tellurics at higher wavelengths. Many of the species we investigate have strong features in this wavelength range (see Fig. 7). We generate template spectra assuming solar abundances over our specified wavelength range using PETITRADTRANS (Mollière et al. 2019) to cross-correlate with our reduced transmission spectra, where the cross-correlation function (CCF) is defined according to equation (13) in Pai Asnodkar et al. (2022). We adopt a Guillot presssure–temperature profile (Guillot 2010) and set the reference pressure such that the resulting continuum of the template spectrum is close to the white-light transit depth. Table 3 lists the planetary parameters that we adopted in constructing all of the template spectra.

We generate individual templates for each species we considered so that any signals in the CCF can be solely attributed to that species. Thus, the abundances of the singular species of interest as well as hydrogen, and helium (since UHJ atmospheres are hydrogen–helium dominated) were inputs in the construction of any given template spectrum. The species that we focus on in this work have been validated as 'detectable' by confirming that they have multiple lines in our wavelength range and yield a peak in the CCF when cross-correlated with observed stellar spectra. For the metal atomic species, we validate the template spectra against the observed spectrum of the host star WASP-12 from our PEPSI observations. For TiO and VO, we validate against archival spectra of GJ 793 (from HARPS-N) and LHS 2065 (from Keck HIRES[4]), respectively, which are M-dwarfs known to display these features (Gray & Corbally 2009). Table 4 specifies the mass mixing ratios adopted based on solar abundance (Palme, Lodders & Jones 2014) and whether or not the species was identified as detectable according to our aforementioned metric.

After the template spectra are generated, they are cross-correlated with the transmission spectra. We conduct SYSREM on the resulting CCF maps, which is more effective than when applied to the reduced transmission spectra. We confirm this by injecting a template spectrum, for example, Fe I, in the in-transit data (before applying any SYSREM) with both nights combined. We scale the Fe I template such that it yields a 5σ signal when SYSREM (1 systematic, 100 iterations) is performed on the transmission spectra before cross-correlation. We find that we are unable to recover this signal if SYSREM is not performed altogether (this is true of all species we tested), likely due to imperfect normalization across observations, whereas we recover an improved 6.83σ signal when SYSREM is performed after cross-correlation. This is because cross-correlation stacks the signal in the transmission spectra that match a given

template spectrum. Thus, it is less sensitive to the stellar line core noise artefacts unless the species of interest has strong stellar absorption lines. Therefore, the streaks are not present in most of the CCF maps. Moreover, SYSREM is more effective at identifying systematics since these maps are smoother than the transmission spectra maps. When we apply SYSREM both before and after cross-correlation, we find the significance of the detection is only improved to 5.18σ, possibly due to the signal being washed out by too many applications of SYSREM. Likewise, increasing the number of systematics to more than one generally does not yield an increase in detection significance. Thus, we adopt one systematic when applying SYSREM after cross-correlation for all species considered except Fe I/II, and Mg I. We use two systematics for these species since their stellar absorption lines are stronger and thus noisier, therefore requiring more SYSREM systematics to minimize correlated noise across observations.

As per standard practice (e.g. Nugroho et al. 2017; Kesseli et al. 2022), we construct SNR maps for a grid of planetary orbital velocities (K_p) and net velocity offset (v_{sys}) values by stacking the in-transit CCFs in the planet's rest frame to get the signal. We define the noise to be the standard deviation of the CCF at velocities beyond $1.5v_{rot}$ away from $0\,km\,s^{-1}$, where v_{rot} is the rotational velocity of the planet assuming it is tidally locked ($9.05\,km\,s^{-1}$). With these definitions, we compute the SNR for a grid of (K_p, v_{sys}) pairs. A single peak with SNR > 5 in this K_p–v_{sys} space qualifies as a detection of the corresponding species.

6.2 WASP-12 b's atmosphere does not display optical absorption

Our search for absorption in the blue arm PEPSI data from various atomic and metal species using both nights of observation does not yield any detections; see Fig. 7. The Mg I map for the first night shows a spurious signal near $K_{pl} = 150\,km\,s^{-1}$ and $v_{sys} = 20\,km\,s^{-1}$. Fig. 8 shows the Mg I cross-correlation maps for Night 1 with the purported absorption track corresponding to the peak of the Mg I SNR map traced out with a black solid line. The signal in the Mg I SNR map for Night 1 could be purely coincidental or an alias with the noisy stellar line cores since the Mg I spectrum in this wavelength range is dominated by just three lines in the triplet between 5167 and 5183 Å. Furthermore, the signal's corresponding value of K_{pl} is nearly $100\,km\,s^{-1}$ less than expected for this planet ($231.5\,km\,s^{-1}$) and thus this signal cannot be attributed the planet's atmospheric absorption.

The Mg I b triplet at 5167, 5172, and 5183 Å is of particular note as a potential tracer of atmospheric escape (Cauley et al. 2019). We do not observe such absorption of planetary origins from either an inspection of the constructed transmission spectra nor cross-correlation. Other lines of potential interest to constraining mass-loss include Ca Iλ4227, Mg Iλ4571, Na D doublet $\lambda\lambda$5890, 5896, and Ca Iλ6122; however, these are outside our wavelength range with the PEPSI cross-dispersers we have chosen for these observations, but can be achieved with others (Keles et al. 2024). In addition to the absorbers presented, we also tested the following atomic and molecular species that are immediately available from the PETITRADTRANS high-resolution opacity database: Al I, B I, Be I, K I, Li I, N I, Na I, Si I, V I, V II, Y I, and VO. These species were deemed undetectable through cross-correlation with an appropriate empirical stellar spectrum (see Table 4). This is because they lack sufficient absorption signal in our wavelength range, with only one or a few lines that are prone to aliasing when cross-correlated.
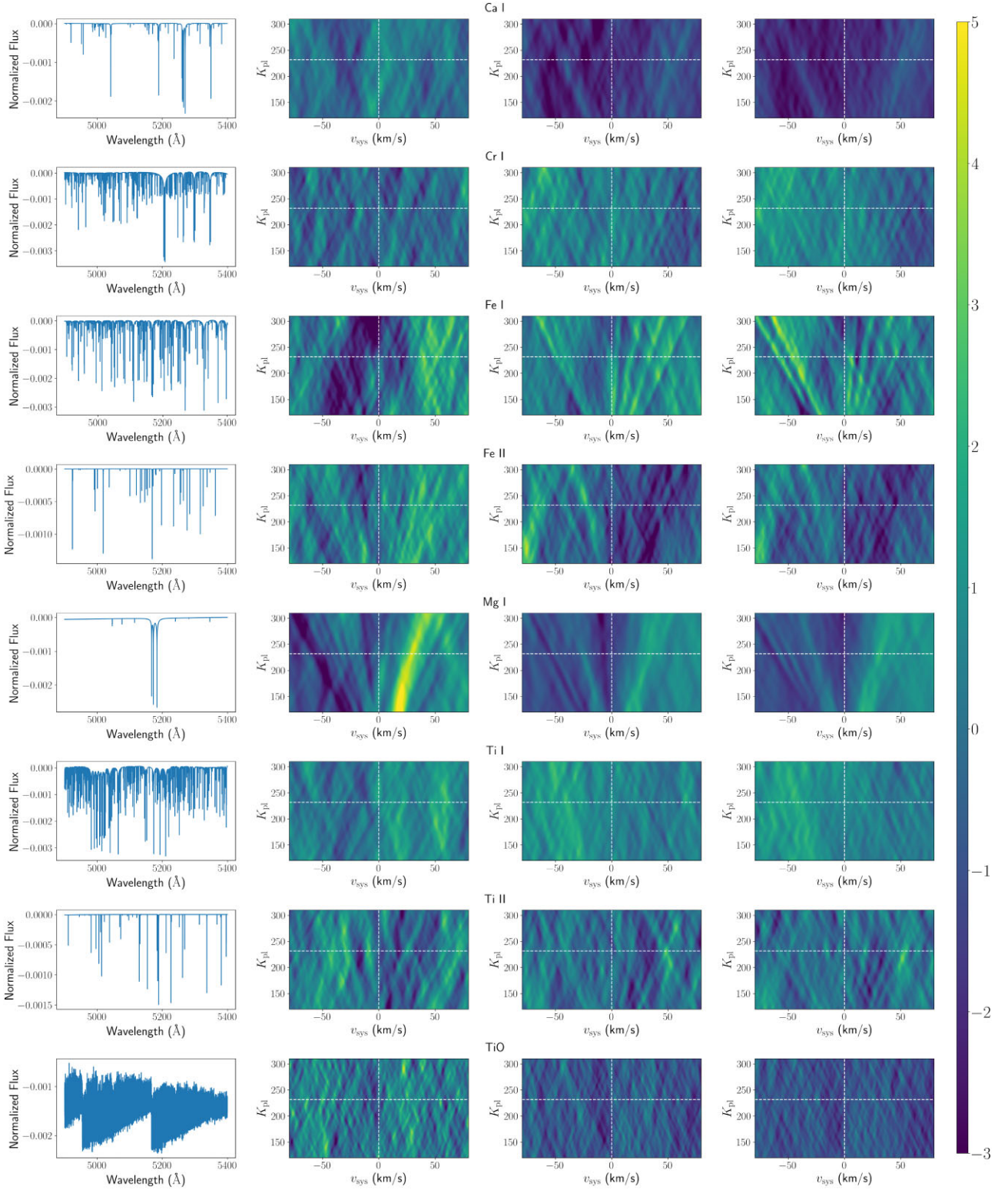
[4] https://koa.ipac.caltech.edu/cgi-bin/KOA/nph-KOAlogin

Figure 7. Columns from left to right – first column: template spectra for a given detectable atomic or molecular species in our wavelength range. Second column column: SNR maps of the corresponding species for Night 1. The dotted white lines correspond to the expected parameters of the system in the absence of velocity shifts from atmospheric dynamics. The colour bar represents SNR from stacking the cross-correlated spectra in a planetary rest frame of the corresponding v_{sys} and K_{pl} combination represented along the x- and y-axes, respectively. Third column: same as the second column, but for Night 2. Fourth column: same as second column, but for both nights stacked. The panels in the last three columns displaying our search for absorption do not show detections from the planetary atmosphere for any of the investigated tracers.

Table 3. PETITRADTRANS planetary parameter inputs.

Parameter	Units	Value	Reference
Planet radius	R_{jup}	1.9	Collins et al. (2017)
Planet mass	M_{jup}	1.47	Collins et al. (2017)
Stellar radius	$R_{\odot}$	1.657	Collins et al. (2017)
Planet surface gravity	m s^{-2}	10.09	Collins et al. (2017)[a]
Mean molecular weight		2.33	
Equilibrium temperature	K	2580	Collins et al. (2017)
Internal temperature	K	100	
Pressure range	Bar	10^{-10}–10^{2}	
Reference pressure	Bar	0.05	
Infrared atmospheric opacity		0.01	
Ratio between optical and IR opacity		0.4	

[a]Derived from reported planetary mass and radius.

Table 4. PETITRADTRANS atomic/molecular abundance inputs and corresponding detectability. Here, detectability of a given species is marked with a check mark if cross-correlation between the template spectrum of the species over the observed wavelength range (PEPSI blue arm) and an appropriate stellar spectrum (i.e. a star known to host absorption features from the species of interest) yields a $>3\sigma$ signal; otherwise, the species is deemed undetectable over the wavelengths of observation and is marked with an 'x'. The variable x in the listed abundances for hydrogen and helium refers to the abundance of the species of interest used in the construction of a given template. All templates were constructed using Kurucz (http://kurucz.harvard.edu/) linelists except for TiO and VO, which came from the ExoMol linelists provided in McKemmish, Yurchenko & Tennyson (2016).

Species	$\log_{10}$ abundance	Detectability
Al I	−5.53	✗
B I	−9.3	✗
Be I	−10.62	✗
Ca I	−5.67	✓
Cr I	−6.36	✓
Fe I	−4.52	✓
Fe II	−4.52	✓
K I	−6.89	✗
Li I	−10.97	✗
Mg I	−4.46	✓
N I	−4.14	✗
Na I	−5.7	✗
Si I	−4.48	✗
Ti I	−7.1	✓
Ti II	−7.1	✓
V I	−8.0	✗
V II	−8.0	✗
Y I	−9.79	✗
TiO	−7.1	✓
VO	−8.0	✗
H	$\log_{10}(0.748 \times (1-x))$	
He	$\log_{10}(0.250 \times (1-x))$	

To compare our non-detections with the literature, we note that Burton et al. (2015), Jensen et al. (2018), and Czesla et al. (2024) are the only other works we could find that conduct high-resolution transmission spectroscopy of WASP-12 b in the optical. In addition to their Hα detection, Jensen et al. (2018) observe planetary Na I absorption via the Na D doublet; Burton et al. (2015) also claims a tentative detection of Na D doublet absorption in the atmosphere of WASP-12 b using defocused transmission spectroscopy. Previous works applied UV spectroscopy to infer metals in WASP-12 b's exosphere such as Na I, Sn I, Mn I/II, Yb II, Sc II, Al II, V II, Mg II (Fossati et al. 2010; Haswell et al. 2012); we are not sensitive to any
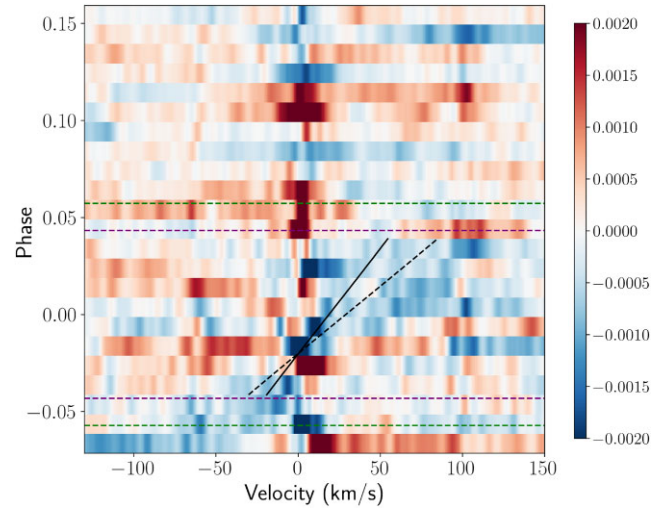
Figure 8. Cross-correlation with Mg I template for Night 1. As before, the green horizontal dashed lines indicate the phases of first and fourth contact while the purple horizontal dashed lines indicate the phases of second and third contact. The black solid line indicates the centre of a purported absorption signature with K_{p} and v_{sys} corresponding to the peak of the Mg I SNR map for Night 1. The black-dashed line corresponds to the absorption track with the highest SNR value of v_{sys} for a K_{p} that matches the projected orbital velocity of the planet. The vertical stationary feature near a velocity of 0 km s^{-1} corresponds to the residual signal from the stellar line core.

of these in our wavelength range. They also suspect the presence of other metals that we have searched for, namely Mg I and Fe I. Fossati et al. (2010) do not provide abundance estimates, so we are unable to consistently constrain the expected observability of their atomic line measurements in our optical wavelength regime. None the less, our non-detections at high-resolution present a challenge to reconcile with UV constraints on WASP-12 b's exospheric composition. Fully understanding this discrepancy will require extensive modelling of the outflow across UV and optical wavelengths. Our non-detections in the optical placed in the context of the literature presents an opportunity to consolidate a holistic, multiwavelength understanding of this system.

We also note that our observations are taken with exposure times of 900 s per spectrum to beat down photon noise. Consequently, the planet changes in RV by $\sim$14 km s^{-1} ($\sim 6\times$ greater than the width of PEPSI resolution element, 2.3 km s^{-1}) over the course of a single observation. Thus, this orbital motion smears out any potential planetary absorption feature, both

Balmer lines and atomic metal lines. This motion blur may drive the absence of atmospheric absorption signatures in our optical data.

6.3 Comparison with other UHJs

The absence of optical absorption features also presents a challenge for comparative planetology of UHJ atmospheres. Atomic metal line absorption from Fe I/II, Cr I/II, Na I, and a plethora of other species has become a characteristic finding in UHJ atmospheres like WASP-76 b, KELT-9 b, KELT-20 b, and more (Casasayas-Barris et al. 2019; Hoeijmakers et al. 2019). At the same time, many UHJs lack such detections despite attempts to search for them with transmission spectroscopy, such as HAT-P-57 b, KELT-7 b, KELT-17 b, KELT-21 b, MASCARA-1b, and others (Stangret et al. 2022). The case of KELT-7 b is particularly noteworthy since this planet is around a star with an effective temperature comparable to WASP-12's. However, KELT-7 b also has a smaller scale height that is less amenable to observation due to its significantly higher surface gravity and lower equilibrium temperature. WASP-12 b is also similar to WASP-76 b and WASP-121 b insofar as their equilibrium temperatures and host star spectral types, yet the latter pair display numerous optical atomic and molecular features in transmission (Seidel et al. 2019; Ben-Yami et al. 2020; Gibson et al. 2020; Hoeijmakers et al. 2020; Cabot et al. 2020b; Kesseli et al. 2022; Pelletier et al. 2022; Sánchez-López et al. 2022b). WASP-76 b has a larger scale height, so this may explain why its atmospheric absorption features are observable when WASP-12 b's are not. However, WASP-121 b may have a scale height smaller than WASP-12 b's depending on the literature value adopted for its equilibrium temperature.

7 CONCLUSIONS

We have presented a search for atmospheric absorption in PEPSI-LBT high-resolution optical transmission spectra of WASP-12 b and report no evidence of planetary absorption features. Our lack of an Hα detection is in direct contradiction with a previous observation at medium resolution in Jensen et al. (2018), but we show that this detection will require exotic phenomena if it is planetary in origin. We conduct injection-recovery tests to constrain the radial extent and escape rate of WASP-12 b's hydrogen envelope. This analysis suggests that we do not have the sensitivity to determine if the hydrogen envelope is confined within the planet's Roche lobe. We explore 1D models of a planetary outflow using the P-WINDS and WIND-Æ codes. The modelled Balmer-line absoprtion features are much smaller in amplitude than the photon noise of our observations as well as the Hα signal purported in Jensen et al. (2018).

From a theoretical standpoint, WASP-12 b possesses qualities that are favourable for observing atmospheric escape. Koskinen et al. (2022) show that even only considering Roche lobe overflow, the system parameters of WASP-12 b suggest that it should have one of the highest mass-loss rates amongst the known planets; this is supported by hydrodynamic outflow inferred from the observed in-transit excess UV absorption. However, the WASP-12 system is fainter than many canonical UHJs observed at high resolution. Our non-detection of Balmer-line absorption with the LBT, a telescope at limit of current facilities with the highest light-collecting area, poses a challenge for further observations of this target at high resolution in the optical. Further investigation of this target with PEPSI will require stacking more observations or observing at lower spectral resolution.

We also search for other optical absorbers including several metal species and TiO. We find no absorption features despite previous inferences of metals in WASP-12 b's exosphere from excess UV absorption in transit. Reconciling WASP-12 b's seemingly barren optical atmosphere in the context of the ever-growing repository of high-resolution detections in UHJ atmospheres will require deeper insight from sophisticated modelling and further observation to tighten empirical constraints.

DATA AVAILABILITY

LBT/PEPSI data analysed in this work will be provided upon request to the corresponding author. HET observations of the WASP-12 system belong to and were provided by contributing author Professor Adam Jensen.

REFERENCES

Akinsanmi B. et al., 2024, A&A, 685, A63
Albrecht S. et al., 2012, ApJ, 757, 18
Alonso-Floriano F. J. et al., 2019, A&A, 629, A110
Astropy Collaboration 2013, A&A, 558, A33
Astropy Collaboration 2018, AJ, 156, 123
Astropy Collaboration 2022, ApJ, 935, 167
Bailey A., Goodman J., 2019, MNRAS, 482, 1872
Barker A. J., Ogilvie G. I., 2009, MNRAS, 395, 2268
Ben-Jaffel L., Ballester G. E., 2014, ApJ, 785, L30
Ben-Yami M., Madhusudhan N., Cabot S. H. C., Constantinou S., Piette A., Gandhi S., Welbanks L., 2020, ApJ, 897, L5
Bonomo A. S. et al., 2017, A&A, 602, A107
Borsa F. et al., 2021, A&A, 645, A24
Burton J. R., Watson C. A., Rodríguez-Gil P., Skillen I., Littlefair S. P., Dhillon S., Pollacco D., 2015, MNRAS, 446, 1071
Cabot S. H. C., Madhusudhan N., Welbanks L., Piette A., Gandhi S., 2020a, MNRAS, 494, 363
Cabot S. H. C., Madhusudhan N., Welbanks L., Piette A., Gandhi S., 2020b, MNRAS, 494, 363
Casasayas-Barris N. et al., 2019, A&A, 628, A9
Cauley P. W., Shkolnik E. L., Ilyin I., Strassmeier K. G., Redfield S., Jensen A., 2019, AJ, 157, 69
Chakrabarty A., Sengupta S., 2019, AJ, 158, 39
Chamberlin P. C. et al., 2020, Space Weather, 18, e02588
Claret A., 2017, A&A, 600, A30
Collins K. A., Kielkopf J. F., Stassun K. G., 2017, AJ, 153, 78
Czesla S. et al., 2024, A&A, 683, 19
Debrecht A., Carroll-Nellenback J., Frank A., Fossati L., Blackman E. G., Dobbs-Dixon I., 2018, MNRAS, 478, 2592
Donati J. F., Semel M., Carter B. D., Rees D. E., Collier Cameron A., 1997, MNRAS, 291, 658
Dos Santos L. A. et al., 2022, A&A, 659, A62
Eastman J., 2012, Astrophysics Source Code Library, record ascl:1206.012
Efroimsky M., Makarov V. V., 2022, Universe, 8, 211
Eggleton P. P., 1983, ApJ, 268, 368
Ehrenreich D., Désert J. M., 2011, A&A, 529, A136
Foreman-Mackey D., 2016, J. Open Source Softw., 1, 24
Foreman-Mackey D., Hogg D. W., Lang D., Goodman J., 2013, PASP, 125, 306
Fossati L. et al., 2010, ApJ, 714, L222
Fossati L., Haswell C. A., Froning C. S., 2011, in Sozzetti A., Lattanzi M. G., Boss A. P.eds, IAU Symp. Vol. 276, The Astrophysics of Planetary Systems: Formation, Structure, and Dynamical Evolution. Kluwer, Dordrecht. p. 163
Fossati L., Ayres T. R., Haswell C. A., Bohlender D., Kochukhov O., Flöer L., 2013, ApJ, 766, L20
Gaia Collaboration 2016, A&A, 595, A1
Gaia Collaboration 2021, A&A, 649, A1
Gibson N. P. et al., 2020, MNRAS, 493, 2215
Gray D. F., 2005, The Observation and Analysis of Stellar Photospheres, 3 edn., Cambridge Univ. Press, Cambridge
Gray R. O., Corbally Christopher J., 2009, Stellar Spectral Classification, Princeton University, Princeton, New Jersey, USA
Guillot T., 2010, A&A, 520, A27
Harris C. R. et al., 2020, Nature, 585, 357
Haswell C. A., 2018, in Deeg H. J., Belmonte J. A.eds, Handbook of Exoplanets. Springer, Cham, Switzerland, p.97
Haswell C. A. et al., 2012, ApJ, 760, 79

Hebb L. et al., 2009, ApJ, 693, 1920
Hill G. J. et al., 2021, AJ, 162, 298
Hoeijmakers H. J. et al., 2019, A&A, 627, A165
Hoeijmakers H. J. et al., 2020, A&A, 641, A123
Huang C., Arras P., Christie D., Li Z.-Y., 2017, ApJ, 851, 150
Huang C., Koskinen T., Lavvas P., Fossati L., 2023, ApJ, 951, 123
Hunter J. D., 2007, Comput. Sci. Eng., 9, 90
Husnoo N. et al., 2011, MNRAS, 413, 2500
Ilyin I. V., 2000, PhD thesis, University of Oulu, Division of Astronomy
Jensen A. G., Cauley P. W., Redfield S., Cochran W. D., Endl M., 2018, AJ, 156, 154
Keles E. et al., 2022, MNRAS, 513, 1544
Keles E. et al., 2024, MNRAS, 530, 4826
Kesseli A. Y., Snellen I. A. G., Casasayas-Barris N., Mollière P., Sánchez-López A., 2022, AJ, 163, 107
Kislyakova K. G. et al., 2016, MNRAS, 461, 988
Kluyver T. et al., 2016, IOS Press, Berlin, Germany. p.87
Kochukhov O., Makaganiuk V., Piskunov N., 2010, A&A, 524, A5
Koskinen T. T., Lavvas P., Huang C., Bergsten G., Fernandes R. B., Young M. E., 2022, ApJ, 929, 52
Kreidberg L., Oklopčić A., 2018, Res. Notes of the Am. Astron. Soc., 2, 44
Li S.-L., Miller N., Lin D. N. C., Fortney J. J., 2010, Nature, 463, 1054
Lodders K., Palme H., Gail H. P., 2009, Landolt Börnstein, 4B, 712
McKemmish L. K., Yurchenko S. N., Tennyson J., 2016, MNRAS, 463, 771
McLaughlin D. B., 1924, ApJ, 60, 22
McKinney W., 2010, in van der Walt S., Millman J.eds, Proceedings of the 9th Python in Science Conference. p. 56
Maciejewski G. et al., 2016, A&A, 588, L6
Maciejewski G. et al., 2018, Acta Astron., 68, 371
Maciejewski G., Niedzielski A., Villaver E., Konacki M., Pawłaszek R. K., 2020, ApJ, 889, 54
Millholland S., Laughlin G., 2018, ApJ, 869, L15
Mollière P., Wardenier J. P., van Boekel R., Henning T., Molaverdikhani K., Snellen I. A. G., 2019, A&A, 627, A67
Mounzer D. et al., 2022, A&A, 668, 18
Murray-Clay R. A., Chiang E. I., Murray N., 2009, ApJ, 693, 23
Nugroho S. K., Kawahara H., Masuda K., Hirano T., Kotani T., Tajitsu A., 2017, AJ, 154, 221
OMG, 2014, Interface Definition Language, Version 3.5.
Oklopčić A., 2019, ApJ, 881, 133
Oklopčić A., Hirata C. M., 2018, ApJ, 855, L11
Pai Asnodkar A., Wang J., Gaudi B. S., Cauley P. W., Eastman J. D., Ilyin I., Strassmeier K., Beatty T., 2022, AJ, 163, 40
Palme H., Lodders K., Jones A., 2014, Solar System Abundances of the Elements. Elsevier Ltd, Amsterdam, Netherlands, p. 15
Patra K. C., Winn J. N., Holman M. J., Yu L., Deming D., Dai F., 2017, AJ, 154, 4
Pelletier S. et al., 2022, BAAS, 54, 100.04
Ramsey L. W. et al., 1998, in Stepp L. M.ed, SPIE Conf. Ser., Vol. 3352, Advanced Technology Optical/IR Telescopes VI. SPIE, Bellingham. p. 34
Rossiter R. A., 1924, ApJ, 60, 15
Sánchez-López A., Lin L., Snellen I. A. G., Casasayas-Barris N., García Muñoz A., Lampón M., López-Puertas M., 2022a, A&A, 666,7
Sánchez-López A., Landman R., Mollière P., Casasayas-Barris N., Kesseli A. Y., Snellen I. A. G., 2022b, A&A, 661, A78
Seidel J. V. et al., 2019, A&A, 623, A166
Seifert W. et al., 2003, in Iye M., Moorwood A. F. M.eds, SPIE Conf. Ser. Vol. 4841, Instrument Design and Performance for Optical/Infrared Ground-based Telescopes. SPIE, Bellingham. p. 962
Smalley B., 2005, Memorie della Societa Astronomica Italiana Supplementi, 8, 130
Smette A. et al., 2015, A&A, 576, A77
Stangret M., Casasayas-Barris N., Pallé E., Orell-Miquel J., Morello G., Luque R., Nowak G., Yan F., 2022, A&A, 662, A101
Strassmeier K. G. et al., 2015, Astron. Nachr., 336, 324
Strassmeier K. G., Ilyin I., Steffen M., 2018, A&A, 612, A44
Tamuz O., Mazeh T., Zucker S., 2005, MNRAS, 356, 1466

Tull R. G., 1998, in D'Odorico S.ed., SPIE Conf. Ser. Vol. 3355, Optical Astronomical Instrumentation. SPIE, Bellingham. p. 387

Turner J. D., Ridden-Harper A., Jayawardhana R., 2021, AJ, 161, 72

Valenti J. A., Piskunov N., 1996, A&AS, 118, 595

Valenti J. A., Piskunov N., 2012, Astrophysics Source Code Library, record ascl:1202.013

Van Rossum G., Drake F. L., Jr, 1995, Python reference manual. Centrum voor Wiskunde en Informatica Amsterdam

Virtanen P. et al., 2020, Nature Methods, 17, 261

Wagner R. M., 2008, in McLean I. S., Casali M. M.eds, SPIE Conf. Ser. Vol. 7014, Ground-based and Airborne Instrumentation for Astronomy II. SPIE, Bellingham. p. 701409

Weinberg N. N., Sun M., Arras P., Essick R., 2017, ApJ, 849, L11

Wiese W. L., Fuhr J. R., 2009, J. Phys. Chem. Ref. Data, 38, 565

Wong I., Shporer A., Vissapragada S., Greklek-McKeon M., Knutson H. A., Winn J. N., Benneke B., 2022, AJ, 163, 175

Wyttenbach A. et al., 2020, A&A, 638, A87

Yan F., Henning T., 2018, Nat. Astron., 2, 714

Yan F. et al., 2021, A&A, 645, A22

Yee S. W. et al., 2020, ApJ, 888, L5

Zhang Y. et al., 2022, A&A, 666, A47

This paper has been typeset from a TeX/LaTeX file prepared by the author.